Electro–thermal modelling of a supercapacitor and experimental validation

Alberto Berrueta, Idoia San Martín, Andoni Hernández, Alfredo Ursúa, Pablo Sanchis*

Department of Electrical and Electronic Engineering, Public University of Navarre, Campus de Arrosadía, 31006 Pamplona, Spain

*Corresponding author. Tel.: +34 948169613; fax: +34 948169884

E-mail address: pablo.sanchis@unavarra.es

Highlights

- A physical-based electro-thermal modelling of a supercapacitor is accomplished.

- The electrical and thermal models are represented alike as equivalent circuits.

- A fitting process for the parameters of both models is developed.

- Validation of the models is performed in various situations proving their accuracy.

- The models are valid for the entire temperature and frequency operating range.

Abstract

This paper reports on the electro-thermal modelling of a Maxwell supercapacitor (SC), model BMOD0083 with a rated capacitance of 83 F and rated voltage of 48 V. One electrical equivalent circuit was used to model the electrical behaviour whilst another served to simulate the thermal behaviour. The models were designed to predict the SC operating voltage and temperature, by taking the electric current and ambient temperature as input variables. A five-stage iterative method, applied to three experiments, served to obtain the parameter values for each model. The models were implemented in MATLAB-Simulink®, where they interacted to reciprocally provide information. These models were then validated through a number of tests, subjecting the SC to different current and frequency profiles. These tests included the validation of a bank of supercapacitors integrated into an electric microgrid, in a real operating environment. Satisfactory results were obtained from the electric and thermal models, with *RMSE* values of less than 0.65V in all validations.

Keywords: Supercapacitor; electric model; thermal model; electric circuit; storage system; electric microgrid.

.

1. Introduction

Electricity is a widely-used form of energy which offers considerable advantages compared to other energy vectors, being easy to convert into other forms of energy and simple to transport [1]. However, its major disadvantage is that it is difficult to store[2–4]. Whilst a broad spectrum of electricity storage technologies are available, the most appropriate one will depend on the application in question [5–8]. For those applications requiring the management of large power peaks with rapid dynamics, those technologies offering the best response include supercapacitors (SCs), flywheels and superconducting magnetic energy storage systems [9–11]. Applications of this type are increasingly in demand due to the growing integration of renewable energies into the electricity grid, the advancement of electric microgrids based on renewable energies and smart loads, the development of electric vehicles, etc. [12–14].

Given the fact that SCs store energy as an electric field, with no need to convert it into another type of energy, this is the most suitable technology to cover those applications requiring the management of rapid power variations. The result is high efficiency and reliability with a simple installation and integration process [15–17]. Supercapacitors are very high surface area activated capacitors that use a molecule-thin layer of electrolyte as the dielectric to separate charge. SCs are formed by two porous electrodes immersed in an electrolyte solution. Both electrodes are separated by an electrically insulating membrane that prevents short circuits. As a result of the extensive contact surface area between the electrode and electrolyte and the small gap between the opposing positive and negative charges, extremely high capacitance values can be obtained [15,18,19]. Electronic double layer capacitors (ELDCs) comprising carbon-based electrodes immersed in a liquid electrolyte, are currently the most developed and used SC technology [20,21], providing a very high power output and longer cycle life than other types of SC, whilst the production process is simpler and the materials used are less expensive. EDLCs are being marketed by companies such as Maxwell Technologies [22] and the Tecate Group [23].

The modelling of the electrical behaviour of SCs has been widely studied in the literature through a number of models used to predict performance. Some are relatively simple [24–27], whilst others are based on more complex mathematical models requiring longer simulation times [28–30]. The classical equivalent circuit is one of the most widely used electric models, comprising a capacitor representing the SC capacitance, a series resistor representing the ohmic losses and a parallel resistor representing the SC self-discharge [24]. This is a useful

model for quick estimate or sizing purposes. However, if a detailed analysis is required or high frequency behaviour needs to be studied, this model is insufficiently accurate, ignoring important physical phenomena such as ion desolvation on penetration in the electrode pores. Zubieta et. al. [31] propose a three branch model, with three parallel-connected branches, each of which is formed by the series connection of a capacitor and a resistor. These branches have different time constants, being the fastest of them of few seconds, the medium of tens of seconds and the slowest time constant of few minutes. Although this model accurately predicts the performance of the SC at low frequencies, it does not model the ion penetration process in the electrode pores or the SC parasitic inductance, both of which are particularly significant during high frequency operation. Mention should also be made of a dynamic SC model developed by Maxwell Technologies Inc. [15], which offers good performance at medium and high frequencies. Its main innovation relates to an RC branch connected in series with the main capacitor, representing the instantaneous response of the SC. Being designed for a high frequency SC operating mode, this model ignores physical phenomena such as ion solvation and desolvation. Devillers et al. [32] published a study comparing the operation of the classical model, branch model and dynamic model in a number of operating environments, concluding that the three models are complementary and that the use of one or the other depends on the specific application. De Levie [28] suggests a complex SC model based on the capacitance of the porous electrodes. The model configuration is based on a distributed capacitance with an electrolyte resistance which is also distributed and which covers the entire depth of each electrode pore. This detailed analysis is suitable in the design process of a SC or in the improvement of its chemical characteristics. However, for simulation purposes, more general models are usually preferred. Torregrossa et al. [33] accurately model the diffusion phenomenon of the supercapacitor residual charge through two current sources. Although this model is extremely accurate for long simulations (2000–4000 s) due to the current sources, it does not model the drop in the SC capacitance observed at high frequencies.

The use of a thermal model to predict the SC temperature has also been widely studied. The SC thermal models can be divided into two broad groups. On the one hand, some studies propose differential equations based on the SC geometry and composition, which are solved either by the finite-differential method [34] or by the finite-element method [35,36]. With these models the inner temperature distribution of each cell can be predicted, nevertheless, for applications in which there is no need for a precise prediction of temperature, the computational cost of these extremely accurate models is too high. On the other hand, there

are comprehensive models where the SC is considered to be a compact, homogeneous body, which are usually represented as equivalent electric circuits. In these models, heat is assumed to be generated uniformly in SC interior. Al Sakka et. al. [37] consider a conduction process inside each cell and a convection process between them. In other studies [38] the authors study the reversible heat generation and calculate experimental model parameters. Chiang et. al. [39] apply extended Kalman filter to SC SOC and temperature estimation. These comprehensive models produce some manageable linear equations for the simulation, with an acceptable accuracy for most applications.

In this paper we model an EDLC, model BMOD0083 manufactured by Maxwell [22] with a rated capacitance of 83 F and rated voltage of 48 V. The aim is to predict its electric and thermal performance based on the physical and chemical phenomena taking place therein. We are therefore proposing an electric model to provide the SC voltage and a thermal model to determine its operating temperature. Each model is represented by an electrical equivalent circuit, making the models easier to understand and allowing them to be readily incorporated into simulation software. A number of experiments served to validate the electric and thermal models developed for a wide range of operating currents, frequencies and temperatures. These experiments included a real operating environment based on the integration of an SC bank in an electric microgrid located at the Public University of Navarre (UPNa).

2. Supercapacitor description and experimental setup

The experimental work reported herein was performed at the UPNa Renewable Energies Laboratory which is equipped with several Maxwell BMOD0083 supercapacitors [22]. Each SC comprises 18 series-connected BCAP1500 P270 cells, each having a rated capacitance of 1500 F and a rated voltage of 2.7 V, giving the BMOD0083 supercapacitor a rated capacitance of 83 F and a rated voltage of 48 V. The EDLC cells comprise two activated porous carbon electrodes, separated by a cellulose membrane, and an organic electrolyte consisting of a quaternary salt tetraethylammonium tetrafluoroborate (TEATFB) solved in acetonitrile (AN). The SC housing is primarily aluminium, for high thermal conductivity, facilitating the dissipation of the heat generated during operation.

Fig.1a shows the SC analysed herein whilst Fig.1b shows the test bench developed to conduct the experimental tasks required. The SC is protected from cell overcurrents, overvoltages and overheating by a circuit breaker (compact NS 160 3P, Schneider Electric)
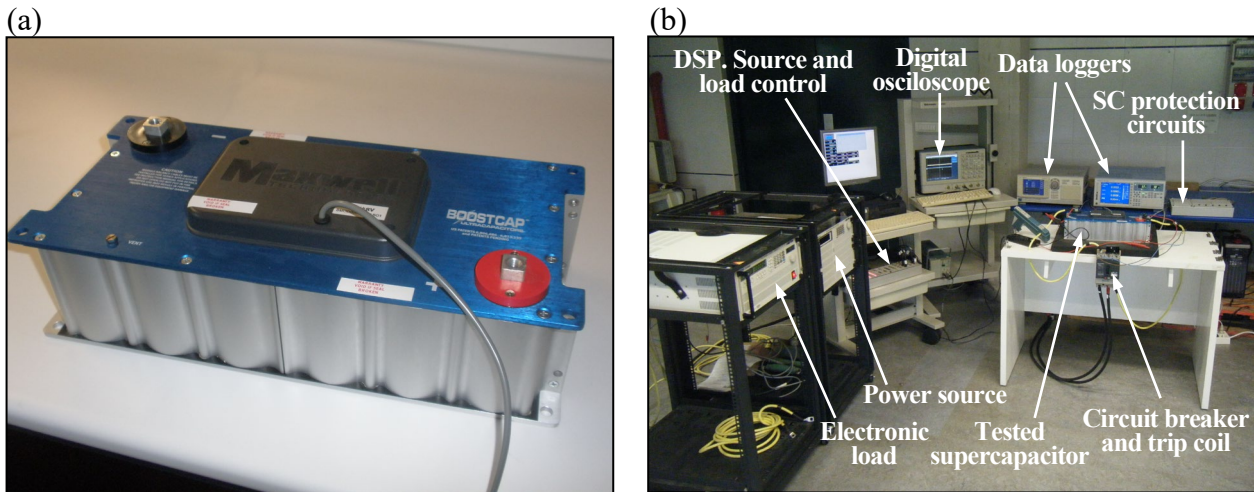
Fig. 1. (a) Photo of the Maxwell SC BMOD0083 (b) SC test bench located in the UPNa Renewable Energies Laboratory.

coupled to a trip coil (TM100DC, Schneider Electric). The SC is connected, through this circuit breaker, to a programmable power source (SPS400x75K12D, Amrel) and a controllable electronic load (PLA4K-400-360-I, Amrel). The current profile supplied or drawn from the SC is externally programmed from a PC through a digital signal processor (DSP, DS 1104, dSpace). A frequency response analyser (FRA, Amrel) is also used in combination with the electronic load in order to perform electrochemical impedance spectroscopy (EIS) test. The analysed physical variables were measured and recorded using two data loggers (WT 1600 and WT 3000, Yokogawa) and a digital oscilloscope (TDS 5034, Tektronix).

3. Electric model

3.1. Double layer effect and charge distribution

The alignment of charges of opposite polarity at the interface between each electrode and the electrolyte in the supercapacitor cells is known as the double layer effect. The electrode charges are electronic whilst those in the electrolyte are ionic [40]. An increase in the voltage applied to this double layer intensifies the electric field in this zone, thereby increasing the force of attraction, compressing the ionic layer and reducing the effective separation distance between the positive and negative charges. Given the small distance already existing between the double layer charges, this gap reduction, leading to a voltage increase, takes on particular importance. Therefore the double layer capacitance increases in line with the voltage applied. Although a number of theoretical expressions model the double layer effect [40,41], empirical

results are used in SC modelling, as they accurately reproduce the behaviour of the phenomenon. Several authors have shown the precision of the following expression, which linearly relates capacitance (C) with the voltage applied at the double layer (v_{dl}) [31,42].

$$C = C_0 + k \cdot v_{dl} \tag{1}$$

where C_0 is the capacitance at 0 V (F) and k is a parameter which multiplies v_{dl} (F V^{-1}). Considering Eq. (1), the current flowing through the double layer (i_{dl}) can be calculated as follows:

$$i_{dl} = \frac{dq}{dt} = \frac{d(C \cdot v_{dl})}{dt} = \frac{d\left((C_0 + k \cdot v_{dl}) \cdot v_{dl}\right)}{dt} = (C_0 + 2k \cdot v_{dl}) \cdot \frac{dv_{dl}}{dt} \tag{2}$$

Based on Eq. (2) the differential capacitance of an SC cell (C_{dif}) is defined as the ratio between the current flowing through the double layer and the variation in the voltage applied to it in relation to time:

$$i_{dl} = C_{dif} \cdot \frac{dv_{dl}}{dt} \longrightarrow C_{dif} = C_0 + 2k \cdot v_{dl} \tag{3}$$

Capacitance (C) and differential capacitance (C_{dif}) are two ways of referring to the relationship between the charge stored in the double layer and the voltage established through the same. The relationship between both capacitances can be obtained from Eqs. (1) and (3) through the following expression:

$$C_{dif} = C + k \cdot v_{dl} \tag{4}$$

C_{dif} is the parameter obtained from experimental tests which linearize Eq. (3) as shown below:

$$C_{dif} = \frac{i_{dl} dt}{dv_{cl}} \approx i_{dl} \cdot \frac{\Delta t}{\Delta v_{dl}} \tag{5}$$

where Δv_{dl} is the double layer voltage variation occurring over time increment Δt. As well as dependence on voltage, the capacitance of an SC cell is affected by the operating temperature, given the fact that a temperature increase causes a growth in the Brownian motion of the ions forming the double layer. As a result, there is a larger separation between positive and negative charges in this double layer, which brings a decrease in the capacitance [43–45].

The distribution of the electric charges over the surface of the double layer is a significant physicochemical phenomenon which determines the area of contact between the electric and

ionic charges and, therefore, the cell capacitance. This capacitance is largely determined by the ratio between the size of the electrolyte ions and the electrode pores [46]. It is important to point out that the solvents used in most electrolytes are polar, leading to molecular interactions with the ions and ion solvation [18]. Fig. 2a shows a schematic diagram of the diameter (Φ) distribution of supercapacitor electrode pores [46]. Pores with a Φ that is less than that of the electrolyte ions are too small for them to access and make no contribution to the supercapacitor capacitance. Whilst those pores with a Φ that is greater than that of the solvated ions are totally accessible to the ions and intermediate pores with a Φ between that of the solvated and non-solvated ions are accessible to the electrolyte ions that have undergone a desolvation process [47]. In this respect, in order to allow the ions to penetrate these intermediate pores there is a need to break down the intermolecular forces established between the ions and the solvent molecules, a process which requires a certain amount of time.

In order to model the charge distribution process, the different electrode pore sizes are taken into account. The pore sizes of the activated carbon used in the manufacture of the SC electrodes are shown in Fig. 2b [48]. For its part, the electrolyte contains dissolved ions $[Et_4N]^+$ and $[BF_4]^-$. Given the fact that the number of electronic charges managed by both electrodes is the same, the number of cations that are either inserted or deinserted in the double layer of the negative electrode is the same as the number of anions in the positive electrode. The slowest ion type performing the insertion and deinsertion process is the one to limit this phenomenon in each SC cell. This behaviour is closely related to the size of the ions given the fact that, the bigger their diameter, the greater the difficulty in penetrating small pores. Given that the size of the cation $[Et_4N]^+$ is 6.7 Å and the anion $[BF_4]^-$ is 4.8 Å, the
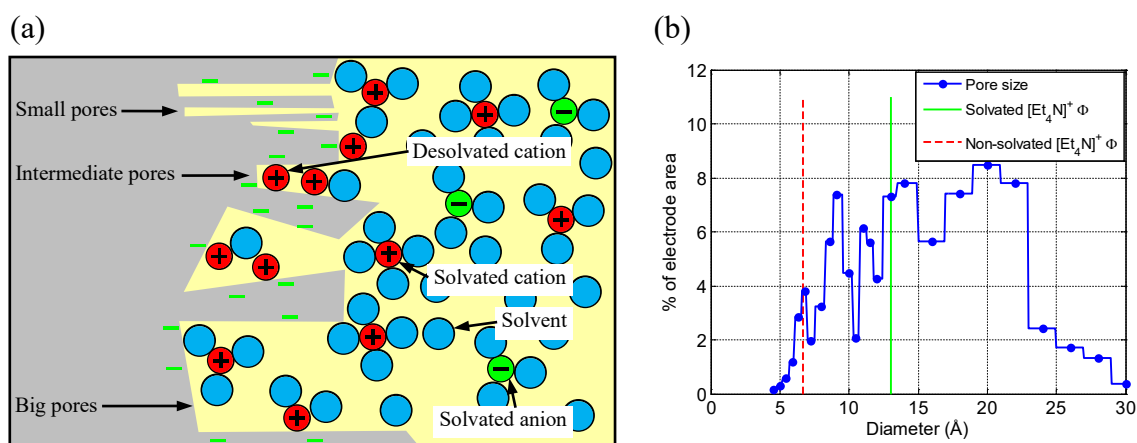

Fig. 2. (a) Schematic diagram of electrode pore size and ion penetration. (b) Pore diameter distribution. With vertical lines solvated and non-solvated $[Et_4N]^+$ ion diameter.

charge distribution process is considered to be limited by [Et$_4$N]$^+$. Fig. 2b uses vertical lines to show its solvated Φ (solid line) with a size of 13 Å, and non-solvated Φ (dashed line) with a size of 6.7 Å. It can be seen that most of the pores have a diameter larger than 13 Å. These large pores are accessible to the electrolyte ions with no need for a prior desolvation process. Therefore ions penetrate into this pore type with no size-related impediment. Intermediate pores (6.7 Å$<\Phi<$13 Å) are accessible to the ions once these have undergone a desolvation process. The smaller the pore size, the higher the number of intermolecular links to be broken down and the longer the time required for this process. Fig. 2b also shows that there are two sizes of intermediate pores which represent the greatest percentage of the electrode area (9 Å and 12 Å). Taking this pore distribution into account, a model is proposed which characterises the concept of capacitance defined in Eq. (1) to refer to the capacitance of a cell (C_{cell}), a parameter represented by capacitive terms C_i (immediate capacitance), C_d (delayed capacitance), and C_l (long term capacitance). Term C_i represents the large pores capacitance ($\Phi >$13 Å), C_d that of the pores with sizes close to 12 Å and C_l that of the pores close to 9 Å. Since capacitance is influenced by temperature only slightly [15], a linear relationship between both magnitudes has been used, which produces an accurate result while maintaining reasonable level of mathematical complexity. Therefore, capacitance C_i was considered to be dependent on the double layer voltage (v_{dl}) and operating temperature (T) based on the following expression:

$$C_i = C_{i0} + C_{i1} \cdot v_{dl} = C_{i0,0} + C_{i0,1} \cdot T + C_{i1} v_{dl} \tag{6}$$

where $C_{i0,0}$ is a capacitance coefficient which is independent of voltage and temperature, $C_{i0,1}$ is a coefficient associated with the thermal dependence of the capacitance and C_{i1} is another coefficient reflecting the dependence of capacitance on voltage. Eq. (6) is valid for temperature values between 0 and 70 ºC. The lower limit is due to the increase in the viscosity of the electrolyte for lower temperatures, which prevents ions penetration into electrode pores and therefore results in a capacitance decrease. The higher limit is the maximum operating temperature for the SC. Given the high proportion of pores bigger than 13 Å in relation to smaller pores in the SC cell electrode (see Fig. 2b), the model proposed considers that the dependency of their capacitance on voltage and temperature has a negligible influence on terms C_d and C_l.

Fig. 3 depicts the physicochemical phenomena analysed in this subsection based on an electrical equivalent circuit. It includes three branches (i, d, l) with their corresponding capacitive terms making up the cell capacitance. In turn, the ion desolvation process required
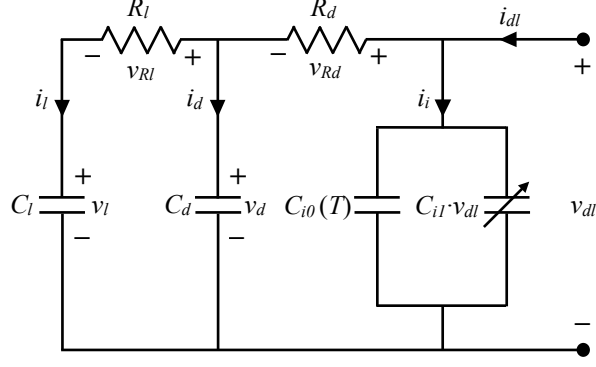
Fig. 3. Equivalent circuit representing the double layer effect and the charge distribution in the electrode pores in an SC cell.

to penetrate the pores with Φ close to 12 Å is represented by resistor R_d, whilst resistor R_l represents the desolvation process to penetrate the pores whith Φ close to 9 Å. Branch i does not include a resistor, as there is no desolvation process.

3.2. Ohmic phenomena and electrical self-discharge

Electronic and ionic charge transport occurs during the SC charging and discharging process [44]. The Joule effect takes place in the electron conductors, whereby part of the electron kinetic energy is converted into heat due to friction with the conductor material. An increase in the operating temperature implies the greater vibration of the atoms in the conductor material which, in most cases, results in an increased Joule effect with temperature. During the ionic charge transport process taking place in the electrolyte, part of the ion kinetic energy is converted into heat due to friction with the other atoms in the dilution. A temperature increase implies an increase in the electrolyte molecule mobility, resulting in a decrease in viscosity. This implies that the energy dissipated by friction decreases as the temperature increases [49]. The voltage required to overcome both dissipative phenomena is proportional to the number of charges transported and, therefore, to current. This proportionality results in these both effects being grouped and called ohmic phenomena. In this respect, the ohmic effect caused by the losses associated with the ion and electron flow through the SC cells is modelled by an electrical resistor (R_s) through which the same current crossing the cell double layer passes, namely i_{dl}, as shown in Fig. 4 (see left electrical drawing). The influence of temperature in this parameter is complex, since the movement of atoms and electrons needs to be modelled. In a trade-off between accuracy and complexity, we have proposed the linear evolution of R_s with the operating temperature (T) based on the following expression:

Fig. 4. Equivalent circuit for the ohmic losses in an SC cell. Ion and electron conduction losses (R_s, left) and membrane losses resulting from self-discharge (R_{leak}, right).

$$R_s = R_{s0} + R_{s1} \cdot T \qquad (7)$$

There are studies which show that the weight of the ionic charge transport is considerably higher than that of the electric charges in the SCs [15]. Since the first effect decreases with increasing temperature, the coefficient R_{s1} must be less than zero. Eq. (7) is valid for a temperature range from 0 to 70 ºC, since the non-linearity of the system has significant effect for higher or lower temperatures [37,44].

Another phenomenon caused by the non-ideality of the SC materials, is electrical self-discharge, due to the fact that the ion conductive membrane separating both electrodes is not a perfect electrical insulator. The self-discharge effect is shown by a linear decrease in the SC voltage. It is represented by electrical resistor (R_{leak}) through which leak current i_{leak} flows, as shown in Fig. 4 (see right electrical drawing).

3.3. Ion penetration into the electrode pores

The porous structure of the carbon electrodes means that, during the SC charging process, the electrolyte ions penetrate these pores to be distributed throughout the entire electrode contact surface. Likewise, during the discharge, the ions must leave the pores and return to the initial SC discharged situation. If the ions are solely located in the more accessible areas of the pores, then the effective capacitance of the SC decreases. For high frequency currents demanded or supplied by the SC, the ion transport process in the electrolyte does not stabilize and the ions are solely located on the pore exterior. This leads to a reduction in the effective capacitance of the SC in high frequency situations, being particularly important in applications in which, for example, the SCs are integrated in switched power converters [49–51].

The effects produced by the ion transport in the SC cell electrodes, is modelled by the RC network shown in Fig. 5. Resistor R_e represents the losses associated with the ion transport from the pore exterior to the electrode-electrolyte interface, whilst the process dynamics are represented by capacitance C_e.

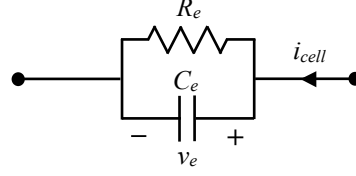Fig. 5. Equivalent circuit representing the ion penetration process in the electrode pores in an SC cell.

3.4. Final configuration of the model

Following the analysis of the various phenomena taking place in a cell, the complete electric model of the SC was configured, based on the electric circuit shown in Fig. 6. Given that the SC is formed by the series connection of a certain number of cells (n_c), it is possible to relate the parameters for this model with the cell parameters, as shown in Eqs. (8) and (9):

$$R_{l,SC} = R_l \cdot n_c, \quad R_{d,SC} = R_d \cdot n_c, \quad R_{s,SC} = R_s \cdot n_c, \quad R_{e,SC} = R_e \cdot n_c, \quad R_{leak,SC} = R_{leak} \cdot n_c \tag{8}$$

$$C_{l,SC} = \frac{C_l}{n_c}, \quad C_{d,SC} = \frac{C_d}{n_c}, \quad C_{i0,SC} = \frac{C_{i0}}{n_c}, \quad C_{i1,SC} \cdot v_{dl,SC} = \frac{C_{i1} \cdot v_{dl}}{n_c} = \frac{C_{i1}}{n_c^2} v_{dl,SC}, \quad C_{e,SC} = \frac{C_e}{n_c} \tag{9}$$

Likewise, the voltages established in the various components of the electric circuit shown in Fig. 6 are related to the analogue voltages of a cell, through factor n_c. On the other hand, given that the cells are series connected, the current flowing through the cells is identical to that flowing through the supercapacitor's equivalent circuit. The series connection of the cells gives the SC a parasitic inductance which is included in the model through inductive parameter L_{SC} as shown in Fig. 6
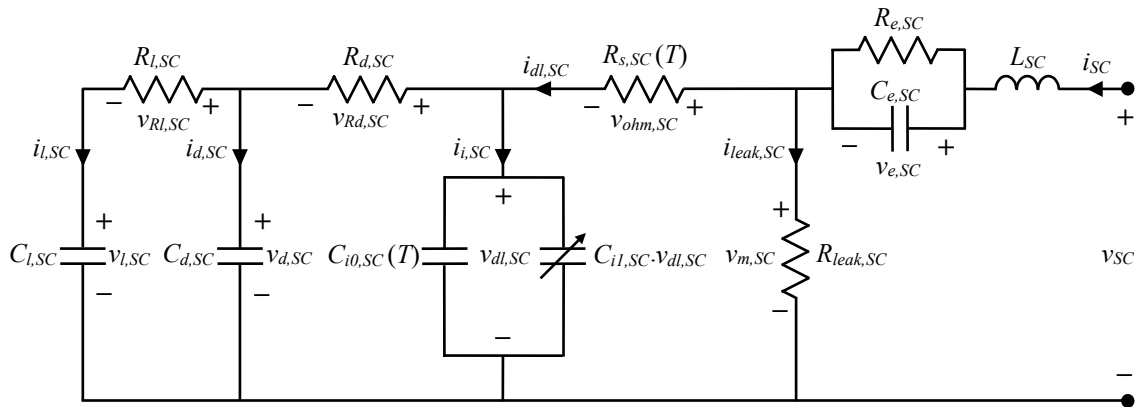

Fig. 6. Electric model of the SC.

4. Thermal model

The thermal energy generated in the SC interior during operation is dissipated into the environment as heat. This energy transfer can be expressed overall through a balance of heating powers [52]:

$$\dot{Q}_n = \dot{Q}_{gen} - \dot{Q}_{ev} \tag{10}$$

In the expression above, $\dot{Q}_{gen}$ is the generated heat, in other words the electric power converted into heat. The term $\dot{Q}_{ev}$ is the dissipated heat from the SC into the environment. $\dot{Q}_n$ is the net heat, contributing to the SC heat energy variation. This heating power conditions the SC temperature variation through the term known as the thermal capacitance (C_{th}):

$$\dot{Q}_n = C_{th} \frac{dT}{dt} \tag{11}$$

Physically, the heat transfer $\dot{Q}_{ev}$ to the environment occurs through a conduction phenomenon from the heat energy generating zone to the SC surface, and a convective phenomenon which transfers this energy to the surrounding air. The capacity of a material to conduct heat is measured by thermal conductivity (λ), which is defined as:

$$\lambda = -\frac{\dot{Q}_{cond}}{S_{cond} \cdot dT/dx} \tag{12}$$

whereby $\dot{Q}_{cond}$ is the heat transferred by conduction, S_{cond} is the transfer surface and dT/dx the temperature gradient. In the case of composite materials, such as the SC, an equivalent thermal conductivity can be calculated for the materials as a whole.

Convection is the heat transfer mechanism occurring in a fluid as a result of the displacement of its molecules. In the case of heat transfer in an SC, this fluid is the air. Heat transfer by convection can be expressed by Newton's Law of Cooling:

$$\dot{Q}_{conv} = h \cdot S_{conv} \cdot (T_S - T_a) \tag{13}$$

where $\dot{Q}_{conv}$ is the heat transferred by convection, h is the convection heat transfer coefficient, S_{conv} is the surface area of the body in contact with the fluid, T_S is the surface temperature of the body and T_a is the ambient temperature.

In the SC thermal model design, the system was considered to be a compact, homogeneous body, bearing in mind that the heat generated is dissipated into the surrounding air, firstly through a conduction process and then through a thermal convection one. In this respect, the SC thermal model has been represented by the electrical equivalent circuit shown in Fig. 7. Heat generation $\dot{Q}_{gen}$ is modelled as a current source dependent on the currents flowing through the resistors of the electric model shown in Fig. 6. The natural conduction and convection processes are modelled as equivalent thermal resistance R_{th} governed by the following expression:

$$R_{th} = R_{cond} + R_{conv} = \frac{l_{cond}}{\lambda \cdot S_{cond}} + \frac{1}{h \cdot S_{conv}} \tag{14}$$

where l_{cond} is the mean length from the heat generating points up to the SC surface. This thermal resistance relates the dissipated heat flow with the difference between T and T_a, as shown in the model in Fig. 7. The analysis of this circuit gives the differential equation which makes it possible to calculate the SC operating temperature:

$$T = T_a + R_{th} \cdot \left[\dot{Q}_{gen} - C_{th} \frac{dT}{dt} \right] \tag{15}$$

The SC dissipated power ($\dot{Q}_{gen}$) is calculated from the electric model shown in Fig. 6 through the following expression:

$$\dot{Q}_{gen} = \frac{v_{e,SC}^2}{R_{e,SC}} + R_{s,SC} \cdot i_{dl,SC}^2 + R_{d,SC} \cdot (i_{d,SC} + i_{l,SC})^2 + R_{l,SC} \cdot i_{l,SC}^2 + R_{leak,SC} \cdot i_{leak,SC}^2 \tag{16}$$

5. Methodology and experimental design to obtain the parameters

This section details the process to obtain the SC electric model (Fig. 6) and thermal model (Fig. 7) parameters implemented in sections 3 and 4 respectively. To do so, three experiments
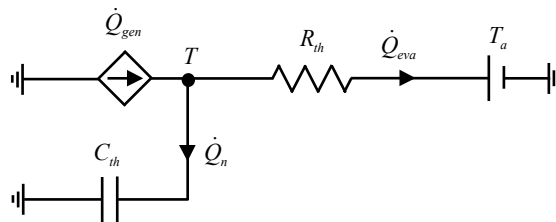

Fig. 7. Thermal model of the SC.

were conducted: *a*, *b* and *c*. Experiment *a* consisted in subjecting the SC to charge and discharge steps from 1V up to 46 V and vice versa, with a value of $i_{SC}=\pm 75$ A for 10 hours, followed by a further 10 hours with the SC idle. In this way, operating temperature *T* increased during the first 10 hours and decreased again during the next 10 hours. Experiment *b* consisted in providing the SC with a charge step of 40A until it reached 41V, followed by a three-day open circuit period. Experiment *c* consisted in conducting an EIS on the SC, maintaining *T* at 30ºC, v_{SC} at 30 V and a steady-state discharge current i_{SC} of 2 A. The amplitude of the sinusoidal perturbation of the small signal current was set at 5% of the steady-state value, and the frequency interval ranged from 10 mHz to 1 kHz.

Based on experiments *a*, *b* and *c,* a five stage method was developed to obtain the parameter values. The first stage consisted in obtaining parameters $R_{s,SC}$, $R_{e,SC}$ and $C_{e,SC}$ through the analysis of the different points at which the charge and discharge steps occur in experiment *a*. Fig.8a shows the evolution of v_{SC} in relation to the charge to discharge step in the experiment, where i_{SC} varies instantaneously from 75 to –75 A. In order to obtain the aforementioned parameters for experiment *a*, we used the simplified electric circuit shown in Fig.8b. Equivalent capacitance $C_{eq,SC}$ represents the SC capacitance at the operating point studied. This parameter needs to be calculated in order to obtain values $R_{s,SC}$, $R_{e,SC}$ and $C_{e,SC}$ for the SC electric model. To do so, we used the v_{SC} slope, as shown in Fig. 8a with a dashed line (slope). The value of $C_{eq,SC}$ is obtained from the following expression:

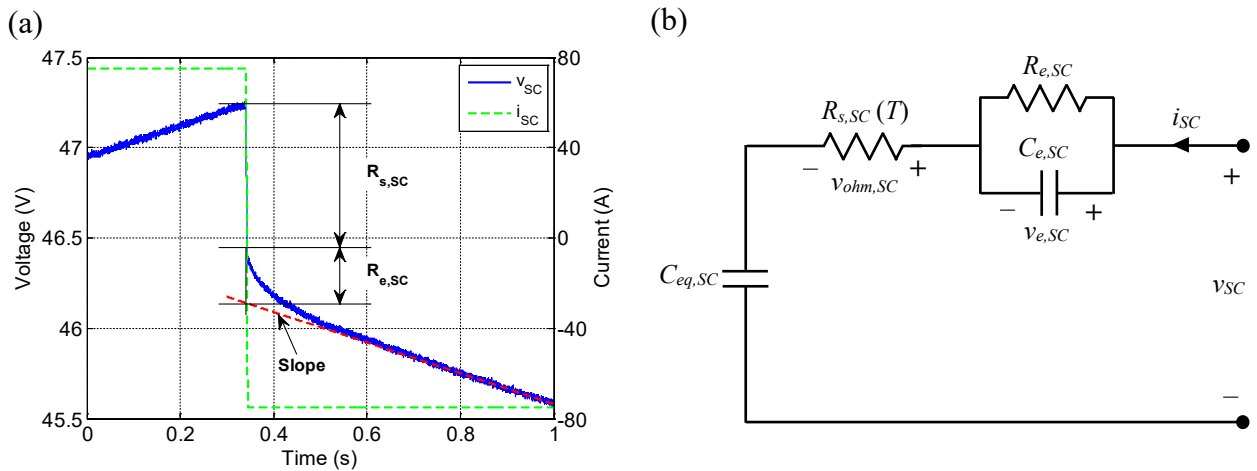$$C_{eq,SC} \approx i_{SC} \frac{\Delta t}{\Delta v_{SC}} \tag{17}$$

(a)

(b)

Fig. 8. (a) SC voltage and current during an interval in experiment *a*. Current step from 75 to –75 A at an operating temperature of 24.2 ºC. (b) Simplified electric circuit considered in order to obtain parameters $R_{s,SC}$ (*T*), $R_{e,SC}$ and $C_{e,SC}$.

The MATLAB® curve fitting toolbox was used to fit the equivalent circuit in Fig. 8b to v_{SC}, taking charge and discharge steps at 16 points with different T values. Fig. 9 shows the parameter fits in relation to T. The fit of $R_{s,SC}$ has a negative slope with temperature whilst a constant evolution is shown for $R_{e,SC}$ and $C_{e,SC}$ as was proposed in section 3. In this way, parameter $R_{s,SC}$ is defined from its coefficients $R_{s0,SC}$=6.6253 mΩ and $R_{s1,SC}$=−2.57·10^{-2} mΩ ºC^{-1} through Eq. (7) and parameters $R_{e,SC}$ and $C_{e,SC}$ take values of 2.4 mΩ and 28.4 F respectively as shown in Table 1.

In the second stage of the fitting method, an approximate value was obtained for parameters $C_{i,SC}$, $R_{d,SC}$, $C_{d,SC}$, $R_{l,SC}$ and $C_{l,SC}$, in addition to a definitive value for $R_{leak,SC}$, which served as a starting point for the iterative fitting process explained in the third stage. To do so, we used the data of experiment b assuming a zero current flowing through certain model elements. Specifically, it was assumed that during the charge process shown in Fig. 10 (from 65 to 150 s) $i_{SC} \approx i_{i,SC}$ given that delayed branch and long-term branch present time constants which are higher than that of the immediate branch by more than one order of magnitude. Using Eqs. (4) and (5), through a fit to the corresponding first order circuit, we obtained an approximate value for $C_{i,SC}$ in relation to $v_{dl,SC}$ at a temperature of 27 ºC whereby $C_{i,SC}^{(1)}$=65.062+0.291·$v_{dl,SC}$ F. On completion of the SC charging process and with the system left as an open circuit, an exponential voltage drop was observed. In this first iteration, it was also assumed that, for the period of time between 150 s and 3·$R_{d,SC}$·$C_{d,SC}$ the discharge of capacitance $C_{i,SC}$ is made through $C_{d,SC}$. In other words, in this time interval $i_{l,SC} \approx i_{leak,SC} \approx 0$ A, given that the time constant for the long-term branch is also higher than that of the delayed
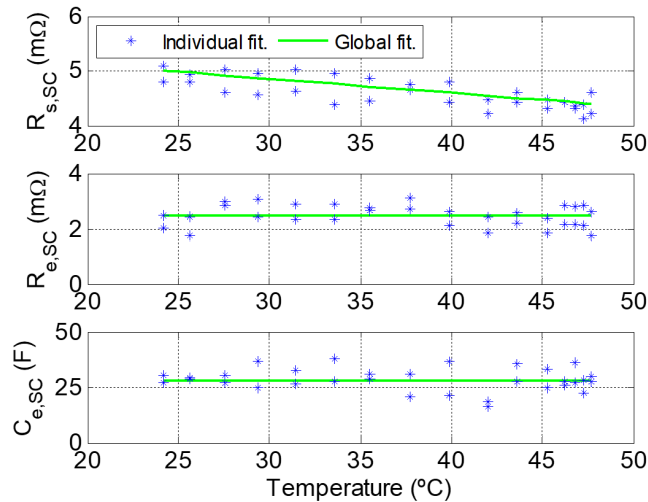

Fig. 9. Fitting of parameters $R_{s,SC}$, $R_{e,SC}$ and $C_{e,SC}$ of the SC electric model in relation to its operating temperature.

Table 1. Value of the parameters for the electric and thermal models of the SC, obtained on completion of the fitting process for the Maxwell SC BMOD0083 (T in ºC). Parameters valid for the studied range of operating temperature (20 ºC–57 ºC).

SC (BMOD0083)	Units
$C_{i0,SC}=69.7527-0.079 \cdot T$	F
$C_{i1,SC}=0.2543$	FV^{-1}
$C_{d,SC}=8.92$	F
$R_{d,SC}=5.21$	Ω
$C_{l,SC}=9.68$	F
$R_{l,SC}=372.02$	Ω
$R_{leak,SC}=169.048$	$k\Omega$
$R_{s,SC}=6.6253-2.57 \cdot 10^{-2} \, T$	$m\Omega$
$C_{e,SC}=28.40$	F
$R_{e,SC}=2.4$	$m\Omega$
$L_{SC}=404$	nH
$R_{th}=0.7086$	ºC W^{-1}
$C_{th}=9670.81$	J ºC^{-1}

branch by more than one order of magnitude. We thus calculated the first approximation of values $R_{d,SC}^{(1)}=14.31$ Ω and $C_{d,SC}^{(1)}=5.0383$ F through a fit with the MATLAB® curve fitting toolbox. In the period of time from $3 \cdot R_{d,SC} \cdot C_{d,SC}$ to $3 \cdot R_{l,SC} \cdot C_{l,SC}$ it is assumed that the discharge incurred by $C_{i,SC}$ and $C_{d,SC}$, already established at the same voltage, occurs through $C_{l,SC}$, considering $i_{leak,SC} \approx 0$, given that $R_{leak} \gg R_l$. In this way, through a fit similar to the previous ones, we obtained the values of $R_{l,SC}^{(1)}=150.23$ Ω and $C_{l,SC}^{(1)}=6.1405$ F. Finally, once sufficient time had elapsed (approximately one day), the exponential trend of the voltage disappeared. From that moment onwards, considering the leakage resistance to be the path for the SC discharges, we obtained a value of $R_{leak,SC}=169.048$ kΩ.

In the third stage of the method, we used experiments a and b to develop an iterative process to allow us to firstly correct the error introduced in the parameters calculated in the previous stage, when ignoring currents $i_{d,SC}$, $i_{l,SC}$ and $i_{leak,SC}$ and, secondly, to study the
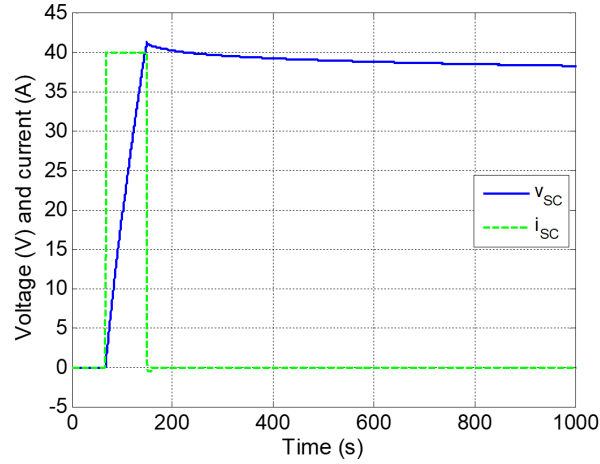
Fig. 10 Detail of the first 1000 seconds of experiment *b*: SC charge at 40 A from 0 to 41 V followed by a 3 day period in open circuit.

variation of capacitance $C_{i,SC}$ with temperature. Firstly, we used a number of charge and discharge sections at 75 A from test *a* at different temperatures. Using the values of the parameters of the electric model calculated in the iteration above, it is possible to calculate the value of $i_{i,SC}$ based on the measurements of v_{SC}, and i_{SC}. Following the corresponding fit of a first order circuit to current $i_{i,SC}$ a value for $C_{i,SC}$ was obtained, being more accurate than the previous iteration. As shown in Fig. 11, for each iteration, data are available taken from different values for *T*, which makes it possible to add the thermal dependence to $C_{i,SC}$. Subsequently, with test *b*, we followed a similar process to that used in the first iteration, with the difference that, in the following iterations, we had an approximate value for the currents passing through each element of the model. In this way we calculated values $R_{d,SC}^{(k)}$, $C_{d,SC}^{(k)}$, $R_{l,SC}^{(k)}$ and $C_{l,SC}^{(k)}$ in the same way as for stage 2, obtaining increasingly more accurate values. After repeating this iterative process between 30 to 40 times, the parameter values converged into the following ones, as summarised in Table 1: $R_{d,SC}$=5.21 Ω, $C_{d,SC}$=8.92 F, $R_{l,SC}$=372.02 Ω, $C_{l,SC}$=9.68 F and term $C_{i,SC}$ is defined by coefficients $C_{i0,SC}$=69.7527– 0.079·*T* F and $C_{i1,SC}$=0.2543 F V^{-1}, as shown by Eq. (6).

In the fourth stage of the method, we obtained the contact inductance L_{SC}, the only electrical parameter still required to complete the model in Fig. 6. To do so, the *c* test was used, consisting in an EIS. The time required to go through the high frequencies of this EIS is very short (Δt<1s for a frequency interval from 10 Hz to1 kHz). This ensures that there is little variation in the SC voltage and that the system is at a stable operating point. The equivalent impedance of the electric model is represented by the following expression:
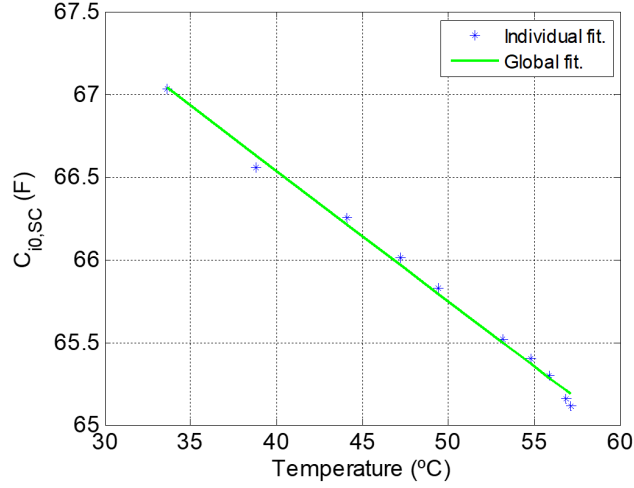
Fig. 11. Linear fitting of $C_{i0,SC}$ in relation to the SC operating temperature, based on the data from experiment *a*.

$$Z = j\omega L_{SC} + \cfrac{1}{\cfrac{1}{R_e} + j\omega C_e} + \cfrac{1}{\cfrac{1}{R_{leak}} + \cfrac{1}{R_s + \cfrac{1}{j\omega C_i + \cfrac{1}{R_d + \cfrac{1}{j\omega C_d + \cfrac{1}{R_l + \cfrac{1}{j\omega C_l}}}}}}} = \text{Re} + j \cdot \text{Im} \qquad (18)$$

All the parameters of the electrical equivalent circuit intervene in Eq. (18), with inductance L_{SC} being the only unknown parameter. In order to obtain the value of L_{SC} the MATLAB® curve fitting toolbox was used to fit Eq. (18) to the data measured in the EIS conducted in experiment *c* as shown in Fig. 12. We therefore obtained a value of L_{SC}=404 nH, as shown in
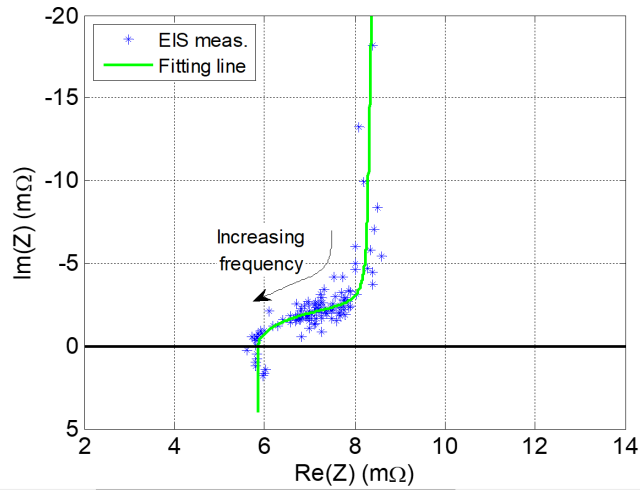

Fig. 12. Nyquist diagram of the EIS conducted on the SC in experiment *c* for a frequency range from 10 mHz to 1 kHz, and fit curve obtained from the equivalent impedance of the SC electric model performance in small signal.
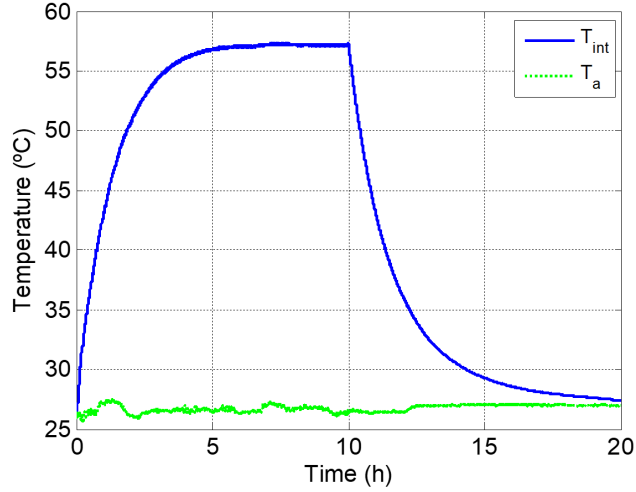
19

Fig. 13. Thermal evolution of the SC in experiment *a*. Heating with heat generation during the first 10 hours and cooling whilst idle during the remaining 10 hours.

Table 1.

In the fifth stage of the method, we obtained the parameters for the thermal model shown in Fig. 7 based on the temperature data for test *a*. Fig. 13 shows the thermal evolution of the heating and cooling processes taking place in the SC during the 20 hour test. For the first 10 hours, the heating power generated by the SC ($\dot{Q}_{gen}$) is considered constant, given that $i_{SC}=\pm 75$ A, whilst in the last 10 hours it is assumed that $\dot{Q}_{gen}=0$ W, given that $i_{SC}=0$ A. The fitting of the heating circuit shown in Fig. 7 is immediate, providing the values of parameters $R_{th}=0.7086$ ºC W^{-1} and $C_{th}=9670.81$ J ºC^{-1} as shown in Table 1.

6. Comparison of experimental and simulated results

6.1. Introduction to the validation of the electro-thermal modelling

The validation of the electro-thermal modelling was based on three experiments in which the SC was made to work in different operating modes. The experiments were programmed on the DSP controlling the electronic charge and the power source. In turn, these experiments were reproduced in MATLAB-Simulink® using the electric model (Fig 6) and thermal model (Fig. 7) in order to compare the results obtained by simulation with the data measured in the said experiments. The input magnitudes for the models are current i_{SC} and temperature T_a. The electric and thermal models interact to reciprocally provide information. While the electric model feeds the thermal model with the electric power loss, the thermal model provides the value of *T*, which allows the electric model to increase its accuracy. The results of the

simulation are voltage v_{SC} and operating temperature T. Thus the operation of the SC is predicted and then compared with the measured results.

6.2. Validation of dynamic behaviour

To make a validation of the dynamic operating mode, the SC was subjected to sinusoidal currents with amplitudes ranging from 15A to 60A and at three different frequencies: 1 Hz, 10 Hz and 100 Hz. The mean value of v_{SC} and operating temperature T remained constant during the test (22.15 V and 25 ºC respectively). Fig. 14 shows the experimental and modelled current-voltage relationships (i_{SC}–v_{SC}) for each frequency with an amplitude of 15 A (a) and 60 A (b). The graphs show how an increase in the i_{SC} amplitude brings with it a greater variation in v_{SC}. On the other hand, it can be seen that, as the frequency increases the slope for the i_{SC}–v_{SC} relationships decreases due to the decrease in the SC equivalent resistance. The area formed in the interior of the i_{SC}–v_{SC} relationships, primarily reflects the SC capacitive behaviour. However, as the frequency increases up to 100 Hz, the area of the i_{SC}–v_{SC} relationships decreases, given the fact that the SC gradually loses its capacitive nature.

For the various current frequencies and amplitudes shown in Fig. 14, the results obtained from the electric model were suitably adjusted to the experimental ones. The validation of the model in this dynamic operating regime was considered to be satisfactory as it shows the capacity of the model to provide reliable results, without an increase in current frequency and amplitude involving significant losses of accuracy. The 15 A amplitude i_{SC}–v_{SC} shown in
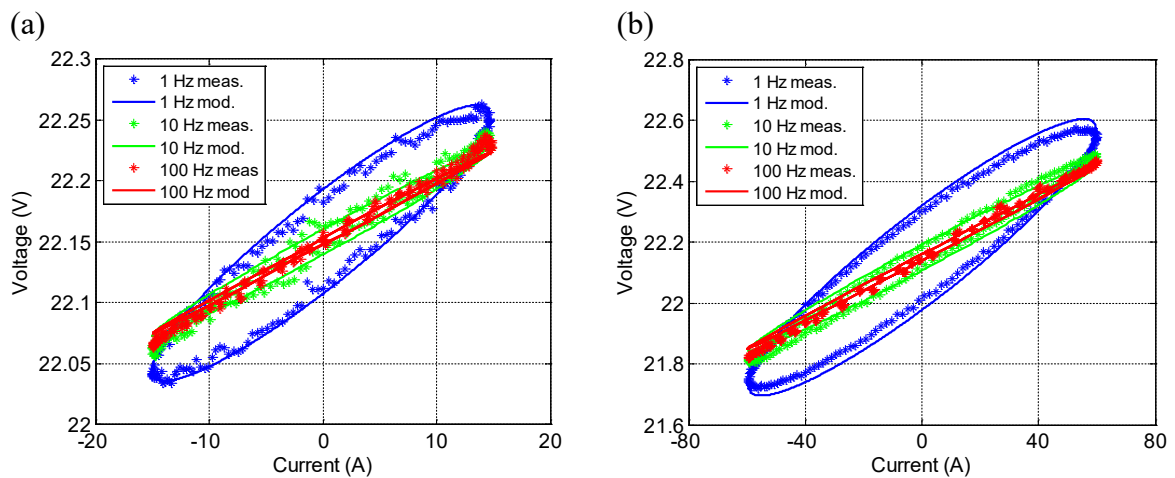

Fig. 14. Validation test for the SC electric model in dynamic mode. Experimental i_{SC}–v_{SC} relationships modelled for a T value of 25ºC and a mean v_{SC} value of 22.15 V. Sine wave currents with frequencies of 1, 10 and 100 Hz and amplitude 15 A (a) and 60 A (b).

Fig. 14a obtained some *RMSE* values under 9 mV whilst the 60 A relationship shown in Fig. 14b provided RMSE values lower than 35 mV.

6.3. Validation of long term operation

Fig. 15 shows the validation of the SC electric and thermal models through a long-term experiment, consisting in a two and a half hour stepped current mode (Fig. 15a), moving continuously from 75 A charging to 75 A discharging and vice versa, causing v_{SC} to oscillate between 2 V and 45 V. Fig. 15b shows the evolution of v_{SC} measured (v_{SC} *meas.*) and modelled (v_{SC} *mod.*) whilst Figs. 15d,e,f show three 300 s zooms, each at different time points in the experiment. In general, high consistency can be observed between v_{SC} *mod.* and v_{SC} *meas.*, with an *RMSE* value in the test of 0.4323 V. The three zooms correspond to three different operating temperatures, that is 28 ºC (Fig. 15d), 40 ºC (Fig. 15e) and 54 ºC (Fig. 15f). In the three zooms, v_{SC} *mod.* accurately fits v_{SC} *meas.*, with *RMSE* values of 0.42 V (Fig. 15d), 0.63 V (Fig. 15e) and 0.49 V (Fig. 15f). These similar *RMSE* values indicate that the dependence of parameters R_s and C_{i0} on T as proposed in the electric model makes it possible to maintain the accuracy of the same in a wide range of SC operating temperatures.

Fig. 15c shows the thermal evolution of the SC throughout the test. While T_a maintains an
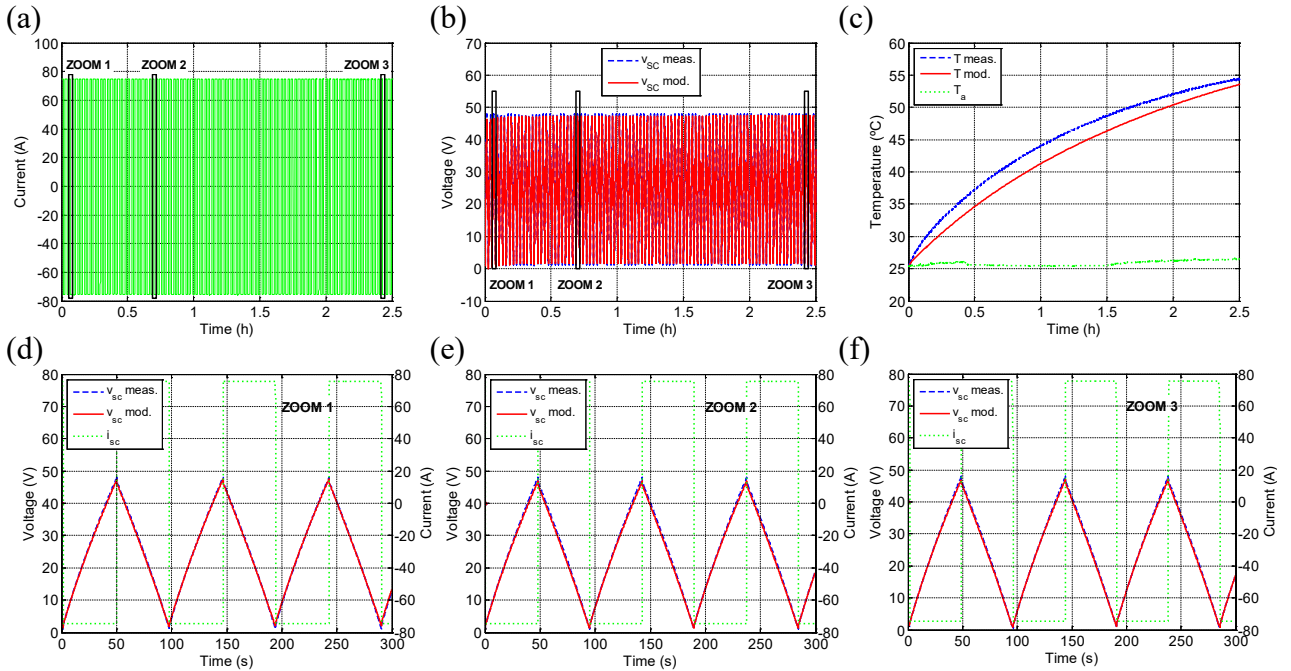

Fig. 15. Endurance test for the SC electro-thermal modelling validation. Test variables: (a) i_{SC}, (b) v_{SC} and (c) T and T_a. Zooms of i_{SC} and v_{SC} at different temperatures: (d) 28 ºC, (e) 40 ºC and (f) 54 ºC.

approximate constant value of around 26 ºC, T increases due to the energy losses taking place in the SC. The thermal model prediction is considered to adequately reproduce the thermal evolution of the SC, given that a 2.229 ºC *RMSE* was obtained. This error is basically due to the simplifications of the actual physical system, which were assumed in order to obtain the thermal circuit of Fig. 7.

6.4. Operation of an SC bank integrated into a microgrid

This subsection validates the electro-thermal modelling in an SC bank operating in a real-life operating environment consisting in an electric microgrid located at the UPNa [53]. The microgrid comprises a hybrid wind-power photovoltaic renewable generating system, a hydrogen based storage system and a power management system (PMS). Fig. 16 shows a diagram of the microgrid component parts. The PV generator has a power of 4 kWp, whilst the wind power generator has 6 kW. The hydrogen based system comprises four series-connected proton exchange membrane fuel cells (PEM FCs) with a total rated power of 4.8 kW. The SC bank comprises three series connected BMOD0083 SCs which, in turn, are connected in parallel directly to the FCs. The microgrid power conditioning system comprises an inverter incorporating the electronic converters. The PMS comprises a PC and a communication bus. Its function is the real time acquisition and control of the microgrid energy flows. In turn, the microgrid has a number of monitoring and measuring devices for electrical and meteorological variables. These variables are stored in a database with a one second frequency. The microgrid consumption is emulated through a programmable
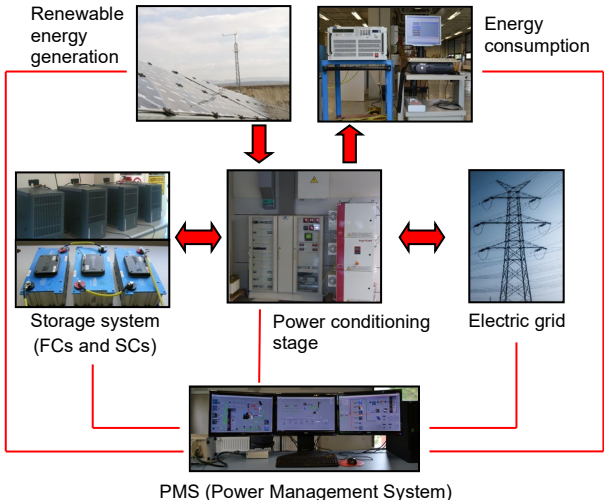

Fig. 16. Schematic diagram of the electric microgrid located at the Public University of Navarre (UPNa).

electronic load, based on actual electricity consumption data measured in a five-member family home located in the vicinity of the UPNa. Likewise, the microgrid also allows for the energy exchange with the electricity grid, depending on the management strategy adopted.

The experiment used for the validation of the electro-thermal modelling of the SC bank is a real microgrid operating interval of 350 s, corresponding to 20:00h on the 12th December 2012, during which there was no power exchange with the electricity grid. Fig. 17 shows the power consumed by the home (P_{con}), the power generated by the renewable system (P_{ren}) and the power supplied by the storage system (P_{SS}) for this time interval. P_{con} has a mean value close to 3 kW in the first 250 s of the test, which then rises to a mean value of approximately 4.5 kW. On the other hand, during the experiment P_{ren} records values between 0 W and 680 W with rapid, random variations inherent in the wind power resource. The storage system assumes the difference between P_{con} and P_{ren}, which is always positive in this case.

Fig. 18 shows the currents and voltage in the storage system, comprising the FCs and SCs for the microgrid power profile represented in Fig. 17. Given that, in this experiment, the storage system is operating as a generator, a change has been made to the sign convention used in the equivalent circuit of Fig. 6. Therefore, the current is positive when it leaves the SCs or FCs and is otherwise negative. Fig. 18a shows the storage system current (i_{SS}). Its variation range goes from a minimum value of 18 A to a maximum of 64 A at the end of the test. Part of this current is supplied by the FCs (i_{FC}) whilst the other part is supplied by the SCs (i_{SC}). The i_{FC} shows a smooth evolution throughout the test, as shown in Fig. 18a, with a mean value similar to the i_{SS}. On the contrary, the i_{SC} current shows more abrupt variations
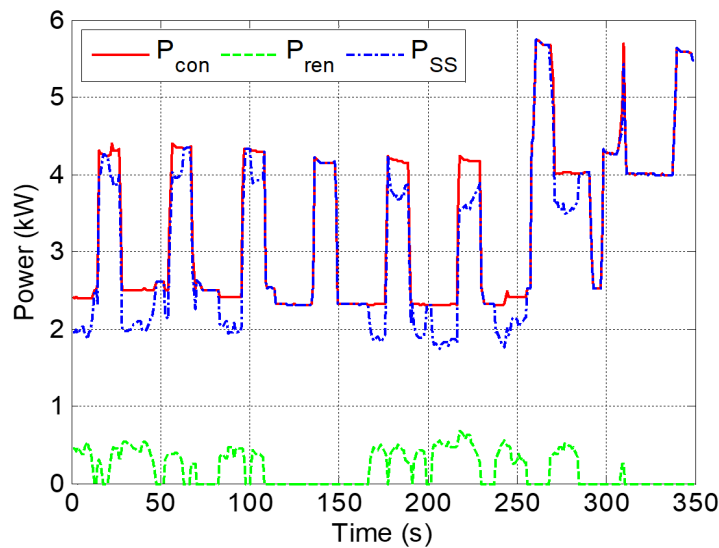

Fig. 17. Power generated by the renewable sources (P_{ren}), power consumed (P_{con}) and power assumed by the microgrid storage system (P_{SS}) corresponding to 20:00h on the 12th December 2012.
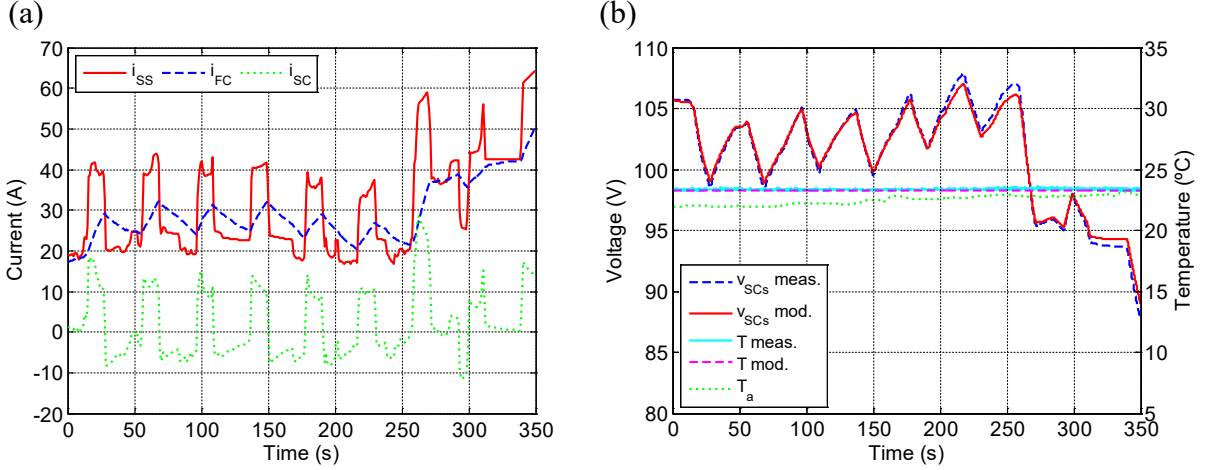
Fig. 18. Experiment and simulation of the integration of a bank of SCs in the microgrid, corresponding to 20:00h on the 12th December 2012. (a) Storage system current (i_{SS}), SCs current (i_{SC}) and FCs current (i_{FC}) and (b) SCs voltage (v_{SCs}), SCs operating temperature (T) and ambient temperature T_a.

and a mean value close to 0 A. In other words, the SCs assume the rapid current variations, allowing the FCs to follow slower dynamics. In this respect, the incorporation of the SCs in the storage system, allows the FCs to operate with slower dynamics, thereby increasing their useful life.

Fig. 18b shows the storage system voltage, which is the same as for the SC bank (v_{SCs}), the SC operating temperature (T) and the ambient temperature of the room holding the storage system (T_a). There are no great changes in v_{SCs} as the FCs do not allow this voltage to fall below 80 V. The maximum value of v_{SCs} during the test is 107 V (t=257 s) and the minimum is 88.5 V (t=350 s). The results obtained with the modelling of the SC bank voltage (v_{SCs} *mod.*) show an adequate and reliable behaviour compared to the voltage measured during the experiment (v_{SCs} *meas.*), with an *RMSE* in the v_{SCs} prediction of 0.457 V. The heating value of the SCs during the test is not very high, as the test was of short duration. Therefore, the thermal model is able to predict the operating temperature with an *RMSE* of just 0.125 ºC. From the analysis in this subsection, it can be concluded that the SC's electric and thermal models are scalable, allowing the connection of a number of SCs and, furthermore, they are accurate when simulating real-time operating environments in an electric microgrid.

7. Conclusions

This paper reports on the electro-thermal modelling of a commercial 83 F 48 V BMOD0083 supercapacitor (SC) by Maxwell, based on the physicochemical phenomena taking place in

each cell. For this purpose, we have presented an electric model and a thermal model in the form of electrical equivalent circuits in which each significant phenomenon is represented. The configuration of the SC electric model is principally based on the following phenomena: double layer; solvation and desolvation of the electrolyte ions; process dynamics of the ion penetration in the electrode pores; ohmic losses; and SC self-discharge. With regard to the thermal model, the SC has been considered to be a compact, homogeneous body which uniformly generates heat throughout. Taking account of the heat conduction and convection processes, the thermal model obtained is able to predict the SC operating temperature in relation to its operating mode. The prediction of the operating temperature has made it possible to introduce a thermal dependence in some of the electric model parameters in order to maintain its accuracy in a wide operating range.

After following the methodology defined in this study to obtain the various parameters for the models, three tests were conducted to validate the models. The first test showed the accuracy of the model when subject to sinusoidal currents of different frequencies and amplitudes, obtaining *RMSE* values of less than 35mV for currents with a 60 A amplitude. The second test validated the models in a 150 minute test with a considerable variation in operating temperature from 25 to 60 ºC, obtaining an *RMSE* for the SC voltage of 0.74 V and 2.229 ºC for the operating temperature. Finally, the third test validated the SC models in a real operating environment. Specifically, a bank of SCs integrated into an electric microgrid was validated, obtaining an *RMSE* for the SC voltage of 0.457 V. Considering the model accuracy and stability shown during this study, these models are a highly useful tool for the sizing, control and performance analysis of many different applications which include SCs.

Acknowledgements

References

[1]   EPRI-DOE Handbook of Energy Storage for Transmission & Distribution Applications, EPRI, Palo Alto, CA, and the U.S. Department of Energy, Washington, DC, 2003.

[2]   B. Dunn, H. Kamath, J.-M. Tarascon, Science. 334 (2011) 928–35.

[3]   E. Hittinger, J.F. Whitacre, J. Apt, J. Power Sources. 206 (2012) 436–449.

[4]   R.M. Dell, D.A.J. Rand, J. Power Sources. 100 (2001) 2–17.

[5]   H. Chen, T.N. Cong, W. Yang, C. Tan, Y. Li, Y. Ding, Prog. Nat. Sci. 19 (2009) 291–312.

[6]   F. Díaz-González, A. Sumper, O. Gomis-Bellmunt, R. Villafáfila-Robles, Renew. Sustain. Energy Rev. 16 (2012) 2154–2171.

[7]   T. Kousksou, P. Bruel, A. Jamil, T. El Rhafiki, Y. Zeraouli, Sol. Energy Mater. Sol. Cells. 120 (2014) 59–80.

[8]   A. Ursúa, L.M. Gandía, P. Sanchis, Proc. IEEE. 100 (2012) 410–426.

[9]   H. Ibrahim, A. Ilinca, J. Perron, Renew. Sustain. Energy Rev. 12 (2008) 1221–1250.

[10]   R. Sebastián, R. Peña Alzola, Renew. Sustain. Energy Rev. 16 (2012) 6803–6813.

[11]   N. Koshizuka, F. Ishikawa, H. Nasu, M. Murakami, K. Matsunaga, S. Saito, O. Saito, Y. Nakamura, H. Yamamoto, R. Takahata, Y. Itoh, H. Ikezawa, M. Tomita, Phys. C Supercond. 386 (2003) 444–450.

[12]   H. Zhou, T. Bhattacharya, D. Tran, T.S.T. Sing, A.M. Khambadkone, IEEE Trans. POWER Electron. 26 (2011) 923–930.

[13]   A. Etxeberria, I. Vechiu, H. Camblong, J.-M. Vinassa, Energy Convers. Manag. 54 (2012) 113–121.

[14]   C.S. Eldridge, Using Super Capacitors to Interface a Small Wind Turbine to a Grid-Tied Micro-Inverter, B.S. Kansas State Univresity, 2011.

[15]   J.M. Miller, Ultracapacitor Applications, 1st ed., The Institution of Engineering and Technology, London, 2011.

[16]   A. Chu, P. Braatz, J. Power Sources. 112 (2002) 236–246.

[17]   D.Y. Jung, Y.H. Kim, S.W. Kim, S.-H. Lee, J. Power Sources. 114 (2003) 366–373.

[18]   I. Hadjipaschalis, A. Poullikkas, V. Efthimiou, Renew. Sustain. Energy Rev. 13 (2009) 1513–1522.

[19]   H. Jin, X. Wang, Z. Gu, J. Polin, J. Power Sources. 236 (2013) 285–292.

[20]   R. Nandhini, P.A. Mini, B. Avinash, S.V. Nair, K.R.V. Subramanian, Mater. Lett. 87 (2012) 165–168.

[21]   G. Yu, X. Xie, L. Pan, Z. Bao, Y. Cui, Nano Energy. 2 (2013) 213–234.

[22]   Maxwell Technologies, http://www.maxwell.com, (2013).

[23]   Tecate Group, http://www.tecategroup.com, (2013).

[24]   P. Sharma, T.S. Bhatti, Energy Convers. Manag. 51 (2010) 2901–2912.

[25]   R.L. Spyker, R.M. Nelms, IEEE Trans. Aerosp. Electron. Syst. 36 (2000) 829–836.

[26]   Y. Wang, J.E. Carletta, T.T. Hartley, R.J. Veillette, 2008 51st Midwest Symp. Circuits Syst. (2008) 726–729.

[27]   T. Wei, X. Qi, Z. Qi, Proceeding Int. Conf. Electr. Mach. Syst. (2007) 69–73.

[28]   R. de Levie, Electrochim. Acta. 8 (1963) 751–780.

[29]   P.J. Mahon, G.L. Paul, S.M. Keshishian, A.M. Vassallo, J. Power Sources. 91 (2000) 68–76.

[30]   R. Martin, J.J. Quintana, A. Ramos, I. de la Nuez, MELECON 2008 - 14th IEEE Mediterr. Electrotech. Conf. (2008) 61–66.

[31]   L. Zubieta, R. Bonert, IEEE Trans. Ind. Appl. 36 (2000) 199–205.

[32]   N. Devillers, S. Jemei, M.-C. Péra, D. Bienaimé, F. Gustin, J. Power Sources. 246 (2014) 596–608.

[33]   D. Torregrossa, M. Bahramipanah, E. Namor, R. Cherkaoui, M. Paolone, IEEE Trans. Ind. Electron. 61 (2014) 1345–1354.

[34]   H. Gualous, H. Louahlia-Gualous, R. Gallay, A. Miraoui, IEEE Trans. Ind. Appl. 45 (2009) 1035–1044.

[35]   K. Wang, L. Zhang, B. Ji, J. Yuan, Energy. 59 (2013) 440–444.

[36]   D.H. Lee, U.S. Kim, C.B. Shin, B.H. Lee, B.W. Kim, Y.-H. Kim, J. Power Sources. 175 (2008) 664–668.

[37]   M. Al Sakka, H. Gualous, J. Van Mierlo, H. Culcu, J. Power Sources. 194 (2009) 581–587.

[38]   H. Gualous, H. Louahlia, R. Gallay, IEEE Trans. Power Electron. 26 (2011) 3402–3409.

[39]   C.-J. Chiang, J.-L. Yang, W.-C. Cheng, J. Power Sources. 234 (2013) 234–243.

[40]   H. von Helmholtz, Ann. Der Phys. 165 (1853) 211–233.

[41]   O. Stern-Hamburg, Z. Elktrochem. Angew. P. 30 (1924) 508–516.

[42]   W. Lajnef, J.-M. Vinassa, O. Briat, S. Azzopardi, E. Woirgard, J. Power Sources. 168 (2007) 553–560.

[43]   E.J. Brandon, W.C. West, M.C. Smart, L.D. Whitcanack, G.A. Plett, J. Power Sources. 170 (2007) 225–232.

[44]   H. Gualous, D. Bouquain, A. Berthon, J.M. Kauffmann, J. Power Sources. 123 (2003) 86–93.

[45]   H. Michel, J. Power Sources. 154 (2006) 556–560.

[46]   G. Gryglewicz, J. Machnikowski, E. Lorenc-Grabowska, G. Lota, E. Frackowiak, Electrochim. Acta. 50 (2005) 1197–1206.

[47]   B. Daffos, P.-L. Taberna, Y. Gogotsi, P. Simon, Fuel Cells. 10 (2010) 819–824.

[48]   D. Qu, H. Shi, J. Power Sources. 74 (1998) 99–107.

[49]   S.I. Fletcher, F.B. Sillars, R.C. Carter, A.J. Cruden, M. Mirzaeian, N.E. Hudson, J.A. Parkinson, P.J. Hall, J. Power Sources. 195 (2010) 7484–7488.

[50]   J. Gamby, P.L. Taberna, P. Simon, J.F. Fauvarque, M. Chesneau, J. Power Sources. 101 (2001) 109–116.

[51]   F. Rafik, H. Gualous, R. Gallay, A. Crausaz, A. Berthon, J. Power Sources. 165 (2007) 928–934.

[52]   Y.A. Çengel, Transferencia de Calor, 2nd ed., McGraw Hill, Mexico D. F., 2004.

[53]   I. San Martín, A. Ursúa, P. Sanchis, Int. J. Hydrogen Energy. 38 (2013) 11655–11671.